

Reverse Austenite Transformation and Grain Growth in a Low-Carbon Steel



THOMAS GARCIN, KEIJI UEDA, and MATTHIAS MILITZER

The mechanisms controlling the reverse austenite transformation and the subsequent grain growth are examined in a low-carbon steel during slow continuous heating. The *ex-situ* metallographic analysis of quenched samples is complemented by *in-situ* dilatometry of the phase transformation and real-time laser ultrasonic measurements of the austenite grain size. Although the initial state of the microstructure (bainite or martensite) has only limited impact on the austenite transformation temperature, it has significant influence on the mean austenite grain size and the rate of grain growth. The coarsening of austenite islands during reverse transformation occurring from the martensitic microstructure is responsible for a large austenite grain structure at the completion of the austenite formation. On the other hand, a much finer austenite grain size is obtained when the austenite transforms from the bainite microstructure. Upon further heating, the rate of austenite grain growth is limited by the presence of nanometric precipitates present in the bainite microstructure leading to a significantly finer austenite grain size. These results give important guidance for the design of thermomechanical-controlled processing of heavy-gage steel plates.

DOI: 10.1007/s11661-016-3855-2

© The Minerals, Metals & Materials Society and ASM International 2016

I. INTRODUCTION

THE demand for extremely thick steel plates has increased significantly in the recent decades. These heavy-gage steel plates are used for the construction of large-scale steel structures such as high-rise buildings, large cargo ships, or ultrahigh-pressure vessels. One of the challenges in the manufacturing of such plates arises from the control of the homogeneity of the microstructure through thickness. It is frequently not possible to apply an adequate amount of deformation during hot rolling limiting the degree of grain refinement in austenite and in the resulting transformation products formed upon cooling.^[1,2] In order to obtain the required balance of strength, ductility, and fracture toughness, an additional heat-treatment cycle in the austenite temperature region is introduced to further control the final properties of the plates. The process parameters for this final heat treatment must be carefully controlled such that the core temperature of the plate reaches the austenite region while minimizing the temperature gradient through thickness to avoid extensive grain growth near the plate surface.

Although the mechanisms controlling austenite grain growth are relatively clearly established, the processes occurring during the formation of austenite from a

martensite or bainite microstructure in low-alloyed steels are not yet fully understood. A significant body of research on austenite formation is available in the literature.^[3–46] Initial microstructures from which austenite formation has been investigated include ferrite–pearlite,^[3–17] ferrite-spheroidized carbide,^[3,7,18–21] and ferrite-martensite, and/or bainite^[22–25] structures. Systematic experimental studies have been conducted on the interaction between ferrite recrystallization and intercritical austenite formation in low-carbon steels.^[27–31] It was found that the heating rate^[32–36] as well as the initial microstructure^[37,38] has a direct influence on the nucleation and growth of austenite during austenitization treatment. In addition, multiple studies have been conducted to model the austenite formation using local equilibrium concept,^[39] cellular automaton,^[40] phase field modeling,^[41,42] and mean field approaches based on the Johnson–Mehl–Avrami–Kolmogorov equation.^[43–45] Clearly, the tempering of the initial microstructure as well as the redistribution of substitutional elements during reheating are important phenomena affecting austenite formation.^[46] This is especially relevant for reheat cycles with slow heating rates where the plate is heat treated for extended periods of time at high temperatures. In low alloy steel, it was shown that the retained austenite islands and/or films present between martensite laths and/or bainite plates possess similar crystallographic orientation when they share the same prior austenite grain.^[47–50] The retained austenite islands can coalesce upon reheating, partially recovering the prior austenite grain structure. In high alloy steel, another mechanism was proposed based on the reversibility of crystal orientation for the austenite–martensite transformations. The reverse austenite will recover the same

KEIJI UEDA, Senior Research Engineer, is with JFE Steel Corporation, Steel Research Laboratory, 1, Kawasaki-cho, Chuo-ku, Chiba, 260-0835, Japan. THOMAS GARCIN, Research Associate, and MATTHIAS MILITZER, Professor, are with the The Centre for Metallurgical Process Engineering, The University of British Columbia, 309-6350 Stores Rd., Vancouver, BC V6T 1Z4, Canada. Contact e-mail: thomas.garcin@ubc.ca
Manuscript submitted May 8, 2016.

Article published online November 7, 2016

crystallographic orientation through a fully nondiffusional martensite transformation.^[51,52] A third and important mechanism relates to the orientation relationship that exists between austenite, bainite, and martensite whereby the formation of austenite can be controlled by variant selection principles.^[53,54] Clearly, the diversity of the aforementioned mechanisms combined with the challenges arising in the *ex-situ* examination of the reverse austenite structure contributes to the poor understanding of this transformation.

Over the last two decades, laser ultrasonics has evolved as a mature sensor technique for the real-time examination of metallurgical processes during complex heat-treatment cycles.^[55,56] In this technique, lasers are used for the generation and detection of broad-band ultrasound pulses in the sample. The ultrasonic properties are then related to the characteristics of the microstructure. The technique is remote operated and nondestructive and gives fast and continuous measurements of the variation of metallurgical parameters. It has already been validated that (i) a direct correlation exists between the mean austenite grain size in low alloy steels and the ultrasonic attenuation,^[57–60] and (ii) static recrystallization as well as phase transformation can usually be monitored in real time through the evolution of the ultrasonic velocity.^[61,62] In this work, laser ultrasonics is employed to examine the influence of the initial microstructure on the reverse austenite transformation and the subsequent grain growth in a low alloy C-Mn steel with a chemical composition typically used for thick steel plates. The evolution of the austenite grain size is measured throughout the heating cycle by the laser ultrasonic technique, and selected measurements are validated by optical metallography on quenched samples. The mechanisms for austenite formation are further investigated by means of electron microscopy.

II. EXPERIMENTAL

The steel used for this study is a laboratory ingot of 50 kg prepared in an induction melting furnace. The steel composition is shown in Table I. Following induction melting, the ingot is reheated at 1523 K (1250 °C) for 2 hours before hot rolling in a pilot mill to obtain a final thickness of 75 mm prior to natural cooling to room temperature. The hot-rolled plate is then homogenized for 100 hours at 1523 K (1250 °C) under vacuum before being naturally cooled to room temperature.

Subsequent heat treatments are conducted on a Gleeble 3500 thermomechanical simulator (Dynamic System Inc. Poestenkill, NY). The system is equipped with the Laser Ultrasonics for Metallurgy (LUMet) system. The technical characteristics of the LUMet

sensor are described in detail elsewhere.^[63] Ultrasonic waveform analyses are conducted using the in-house software CTOME.^[64] Tests are conducted using sheet samples of 60-mm length, 10-mm width, and 2-mm thickness. Figure 1 shows the schematic of the heat-treatment cycles that consist of two successive stages. Different paths are designed for the first stage in order to generate four different initial microstructures for the 2nd stage of the heat cycle. The first path of the treatment consists of heating the sample up to 1523 K (1250 °C) at a rate of 100 K/s followed by holding for 60 seconds in order to generate a coarse austenite grain structure. The sample is then gas-quenched at a cooling rate of 60 K/s either to room temperature in order to form a coarse martensite microstructure (CM) or to 773 K (500 °C) where the sample is held for 300 seconds to decompose the austenite into a coarse bainite microstructure (CB) prior to further cooling to room temperature. In the second set of paths, the samples are only brought to 1173 K (900 °C) for 1 seconds in the 1st stage and then quenched directly to room temperature to form a fine martensite microstructure (FM) or held at 773 K (500 °C) for 300 seconds to form a fine bainite microstructure (FB). In the nomenclature adopted for these four parent microstructures, the words coarse and fine refer to the prior austenite grain size. These prior austenite grain sizes are quantified in selected samples after quenching for 1 seconds at 1173 K (900 °C) and 60 seconds at 1523 K (1250 °C). After the completion of the first stage of the heating cycle, the samples are reheated at a rate of 50 K/s to 973 K (700 °C) and then continuously heated to 1273 K (1000 °C) at a rate of 0.3 K/s during which the austenite grain-size evolution is measured *in situ* with LUMet. The selected samples are then quenched at temperatures of 953 K, 1043 K, 1123 K and 1273 K (680 °C, 770 °C, 850 °C and 1000 °C) to also metallographically evaluate the states of the microstructure before and during the reverse austenite transformation as well as the austenite grain sizes at the

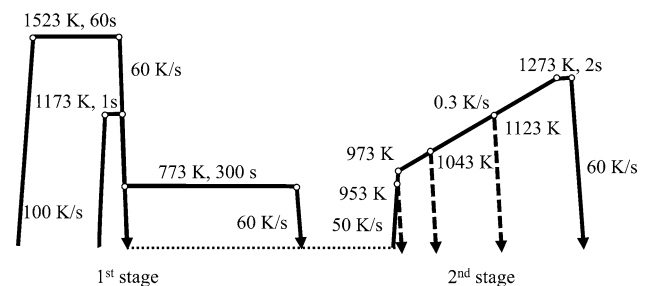


Fig. 1—Schematic of the pre-heat treatment to control the parent microstructures (1st stage) and the subsequent continuous heating tests (2nd stage) indicating the temperatures at which the selected samples are gas-quenched.

Table I. Chemical Composition of the Steel (Wt Pct)

C	Si	Mn	P	S	Al	N
0.17	0.14	2.0	0.004	0.001	0.03	0.003

completion of the transformation and at the maximum temperature of the 2nd stage of the cycle. The temperature is measured using a K-type thermocouple spot welded in the center of the sample. The austenite transformation kinetics is recorded with a contact dilatometer. The samples quenched from the austenite region are later heat treated in a tubular furnace at 773 K (500 °C) for 24 hours under argon atmosphere in order to facilitate revealing the prior austenite grain boundaries by chemical etching. Metallographic observations are conducted in the plane coinciding with the thermocouple position which corresponds to the area probed by the laser ultrasonic sensor and contact dilatometer. Conventional grinding and polishing techniques are applied for the metallography. Nital reagent composed of 3 pct nitric acid in denatured ethanol is used for the observation of the transformed structures resulting from the 1st stage of the heating cycle. Saturated aqueous solution of picric acid is used for the observation of austenite grain structure in the samples quenched from the austenite region during the 2nd stage of the cycle.

The mean equivalent area diameter (EQAD) of austenite grains is quantified from image analysis of at least 500 grains. The sample quenched from the intercritical temperature region are further characterized using a ZEISS-SIGMA field-emission scanning electron microscope (Carl Zeiss SMT Ltd. Germany) equipped with an electron backscattering diffractometry system (EBSD-EDAX, Mahwah, NJ). The acceleration voltage used for the EBSD investigation is 20 kV with a working distance of 10 mm. The EBSD maps are obtained using a square grid with a step size of 50 nm. The OIM™ (TSL) software is used for processing of the EBSD data. A first cleaning of the orientation map is applied using the OIM confidence index standardization method followed by grain dilation where the minimum misorientation between grains is 5 deg with at least 3 pixels per grain. The kernel average misorientation (KAM) is calculated for each map as the average misorientation between a point on the measurement grid and its 1st nearest neighbor. To focus on local rotation, misorientations higher than 5 deg are excluded from the average.

The volume fractions of the phases present in the parent microstructure (α -Fe, γ -Fe, and Fe₃C) are measured by X-ray diffraction (XRD) using the Rietveld quantitative phase analysis. The XRD studies were conducted using a Rigaku RINT-RAPIDII-R micro-diffraction XRD system equipped with a cobalt anticathode ($K_{\alpha} = 0.179$ nm) operating at a voltage of 45 kV and a current of 160 mA, with the integration time being set to 60 seconds.

Nanometric precipitates are identified using a JEOL JEM-3000F transmission electron microscope (TEM) equipped with a Thermo Noran energy dispersive X-ray spectroscopy (EDS) system and operated at an accelerating voltage of 300 kV. The specimens for TEM observation are prepared by ultramicrotomy, *i.e.*, a system using a diamond knife capable of cutting specimens into thin slices. A first slice of 2 mm by 2 mm is embedded in epoxy resin (EPON 812 RESIN) in order to extract a slice with a final thickness of about 30

to 60 nm. The sliced specimen is supported on a conventional copper mesh with a diameter of 3 mm, equipped with a carbon micro-grid.

III. RESULTS

A. Initial Microstructures

Based on the metallographic observation after the first heating cycle, the coarse austenite grain size is determined to be 250 μm , whereas the fine austenite grain size is found to be 10 μm . Four distinct microstructures are obtained from these two austenitization conditions by cooling at a rate of 60 K/s to either the room temperature or the holding temperature of 773 K (500 °C). Figure 2(a) depicts the evolution of the dilation measured during cooling to room temperature at a rate of 60 K/s, *i.e.*, fine and coarse martensites. The austenite fraction transformed shown in Figure 2(b) is calculated by application of the lever rule on dilatometry measurements assuming a law of mixture for linear thermal expansion of austenite and ferrite in the intercritical region.^[65] The austenite start decomposition temperatures, defined as 5 pct transformed, are 703 K and 843 K (430 °C and 570 °C) for the coarse- and fine-grained austenitizing conditions, respectively. The transformation curve measured in the case of fine-grained austenite (FM) depicts a two-step behavior suggesting that the austenite starts to decompose into bainite in the early stage of the transformation. The austenite decomposition then continues with the formation of martensite at lower temperatures. The two-step transformation is not observed during the decomposition of the coarse-grained austenite (CM). For the second heat path designed to produce the fully bainite microstructure, the austenite transformation is controlled by maintaining the holding temperature at 773 K (500 °C). Dilatometry measurements (not included) show that the austenite decomposition has already begun during the course of cooling from a temperature of 848 K (575 °C) in the case of the fine-grained austenite, whereas, in the case of the coarse-grained austenite, the austenite decomposition only begins during isothermal holding. However, the transformation is completed prior to the end of holding at 773 K

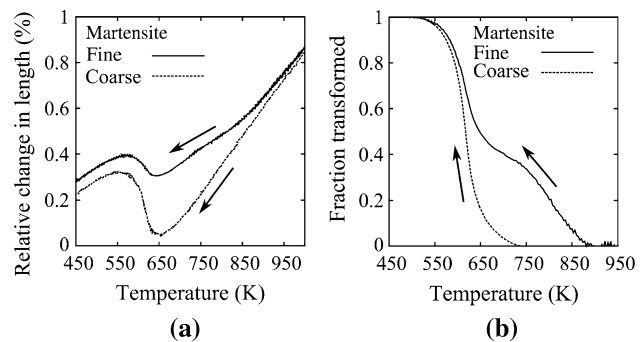


Fig. 2—(a) Dilation and (b) austenite fraction transformed measured during cooling to room temperature at 60 K/s from the coarse-grained (dashed line) and fine-grained (continuous line) austenite.

(500 °C) in both the cases of fine- and coarse-grained austenites, *i.e.*, linear contraction was measured during the subsequent cooling from 773 K (500 °C) to room temperature.

Secondary electron micrographs of the Nital-etched microstructures resulting from the four heating cycles of the 1st stage are shown in Figure 3. The martensite transformed in the sample cooled directly to room temperature from the fine-grained austenite (Figure 3(a)) is composed of small packets of bainite in a matrix of fine martensite needles (FM). The location of selected bainite packets (B) is indicated with white arrows in Figure 3(a). Although the small cementite particles precipitating within the bainite packets are not detected at the magnification shown in Figure 3(a), the presence of bainite is consistent with the dilation measurements showing a two-step transformation (see Figure 2) with the first transformation stage in the temperature range of bainite transformation. No bainite transformation product is visible from the coarse-grained austenite sample (Figure 3(c)), for which the decomposition of austenite initiated at a much lower temperature. Coarse laths of martensite are observed throughout the structure with white constituents present between laths, which are indicative of carbon-rich films arising from the incomplete austenite decomposition. The bainite microstructures transformed from the fine-grained austenite (Figure 3(b)) and the coarse-grained austenite (Figure 3(d)) also have different morphologies. Irregular bainitic-ferrite grains have

transformed from the fine-grained austenite; cementite particles (white constituents) have precipitated primarily along the grain boundaries of bainitic-ferrite grains. On the other hand, cementite islands are homogeneously distributed in the structure and aligned with the bainite laths for the sample cooled from the coarse-grained austenite. The positions of the prior austenite grain boundaries are detected for both the coarse martensite and bainite microstructures by the growth directions of the martensite lath and bainite plates, respectively (dashed lines in Figures 3(c) and (d)).

The coarse martensite and bainite microstructures are further characterized by X-ray diffractometry to identify potential differences between martensite and bainite with respect to the retained austenite and cementite that will control the onset of the reverse austenite transformation. Figures 4(a) and (b) shows the X-ray intensities measured with respect to the scattering angle for the coarse martensite and bainite microstructures, respectively, and their comparison with the expected characteristics for α -Fe, γ -Fe, and Fe_3C . High intensity peaks of α -Fe are measured in both structures. The width of the peak for the martensite structure is wider than that for bainite indicating a higher degree of microstrain in the martensite structure. Measurable peaks of retained austenite are indexed in the coarse martensite (Figure 4(a)) giving a fraction of about 1 pct, and only traces of cementite are detected under this condition. In the case of the coarse bainite (Figure 4(b)), the peaks for cementite are of small intensity but are indexed in the whole range of scattering angles. The fraction of cementite is about

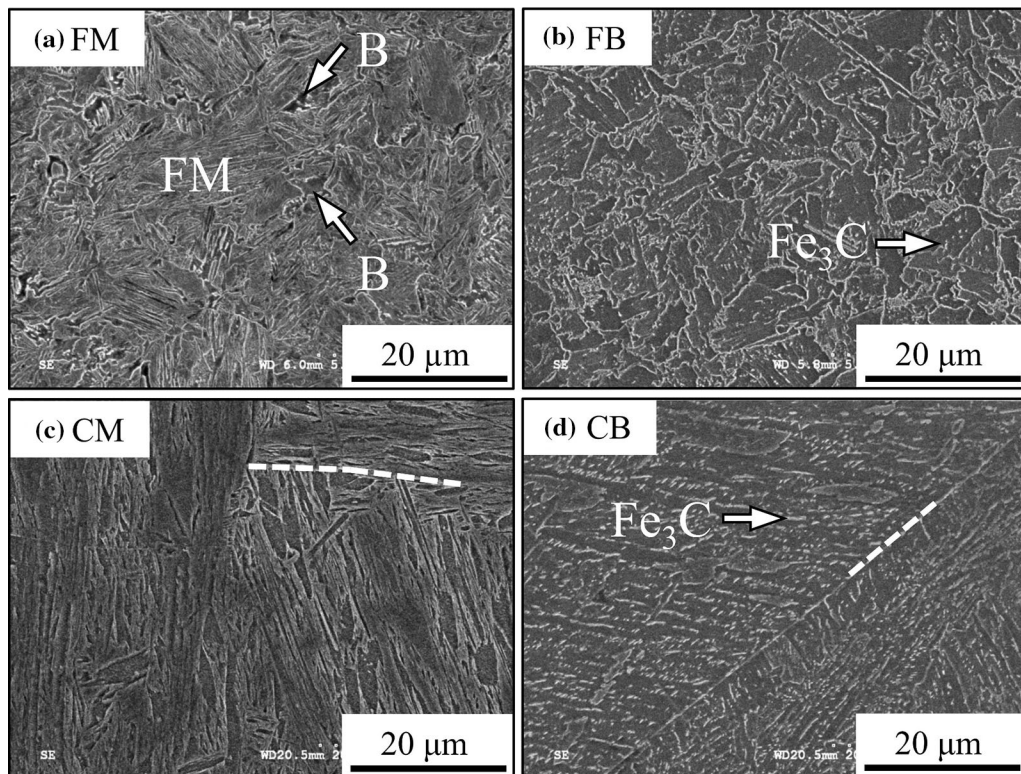


Fig. 3—SEM micrographs of the microstructures resulting from the 1st stage of the heating cycle: (a) fine martensite (FM) cooled from 1173 K (900 °C) to room temperature, (b) fine bainite (FB) cooled from 1173 K (900 °C) and isothermally held at 773 K (500 °C), (c) coarse martensite (CM) cooled from 1523 K (1250 °C) to room temperature, and (d) coarse bainite (CB) cooled from 1523 K (1250 °C) and isothermally held at 773 K (500 °C).

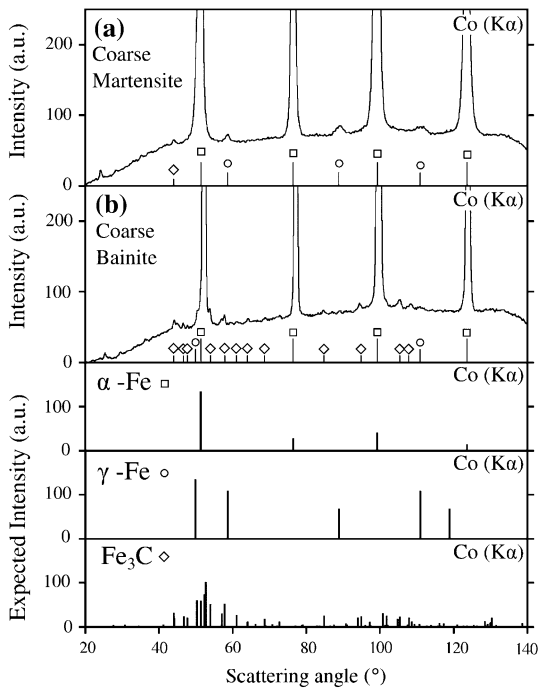


Fig. 4—Intensity of X-ray diffraction for the K α radiation of Cobalt with respect to the scattering angle measured in the (a) coarse martensite and (b) coarse bainite microstructures. The expected positions of the peaks for α -Fe, γ -Fe, and Fe₃C are indicated in the bottom graphs.

1 pct, and only small traces of the retained austenite are detected under this condition. The X-Ray study indicates that the onset of reverse austenite formation is expected to be primarily controlled by the retained austenite in martensite and by the cementite in bainite. X-ray diffractometry is not conducted for the fine martensite microstructures as it contains also some bainite.

B. Tempering Prior to Reverse Austenite Transformation

Tempering of the parent martensite microstructure occurs prior to the nucleation of the reverse transformed austenite during the subsequent reheating in the 2nd stage, thereby modifying the condition for the reverse transformation. A selected sample is therefore quenched during re-heating at a temperature of 953 K (680 °C), *i.e.*, just below the A_{c1} temperature. Figure 5(a) shows the TEM micrograph of the sample with a tempered coarse martensite microstructure. Selected area diffraction pattern of the zone highlighted with the white arrow in Figure 5(a) indicates the presence of cementite in the matrix. The fraction of cementite can hardly be estimated from this analysis, but as a complementary analysis, it confirms the presence of cementite prior to the formation of the reverse austenite from the parent coarse martensite microstructure.

C. Reverse Austenite Transformation

The evolution of the austenite volume fraction during the reverse austenite transformation is obtained from dilation measurements using the lever rule method. The

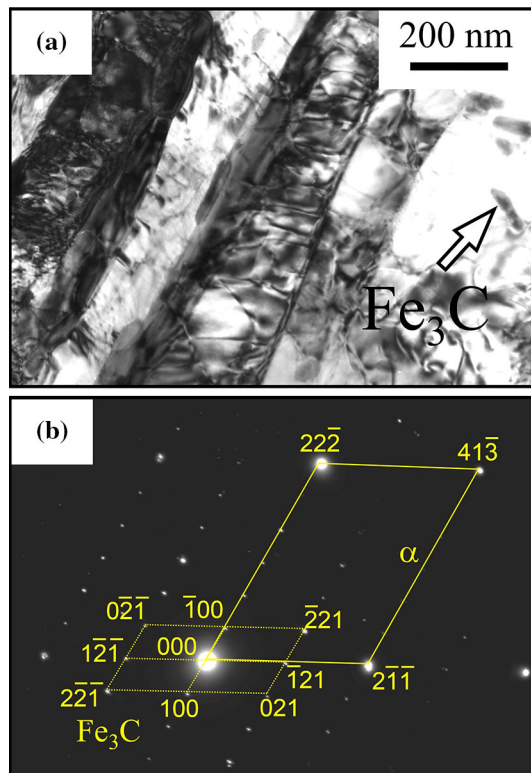


Fig. 5—(a) Thin foil TEM micrograph obtained after reheating the parent coarse martensite microstructure at a rate of 50 K/s to 953 K (680 °C) and Helium gas quenching. (b) Selected area diffraction pattern of the zone highlighted with the white arrow in (a).

dilation measurements and austenite fraction transformed measured upon heating are shown in Figures 6(a) and (b) as a function of temperature for each parent microstructure. The reverse austenite transformation temperature and kinetics are very similar for all the investigated parent microstructures, and austenite transformation is completed at 1113 K (840 °C) for all cases. Substantial tempering and grain growth are occurring during the reverse austenite transformation at a heating rate of 0.3 K/s. The selected samples are therefore quenched from 1043 K (770 °C), where the austenite fraction is approximately 0.5, to allow for the observation of the partially transformed microstructures.

Figure 7 shows the SEM micrographs of these partially transformed samples for the parent fine martensite (Figure 7(a)), fine bainite (Figure 7(b)), coarse martensite (Figure 7(c)), and coarse bainite (Figure 7(d)). The untransformed microstructure has experienced partially tempering during heating up to 1043 K (770 °C). The reverse-transformed austenite decomposed into fresh martensite during the rapid quenching from the inter-critical region. A small fraction of the reverse-transformed austenite may remain untransformed at room temperature after the quenching from 1043 K (770 °C). SEM observations of the microstructures obtained for the fine martensite (Figure 7(a)) and fine bainite (Figure 7(b)) samples present similar microstructural features with a fine and homogeneous mixture of

tempered martensite (TM) (darker constituent) and fresh martensite (FrM) (light gray constituent). The microstructure observed in the sample with the parent coarse martensite consists of two different classes of

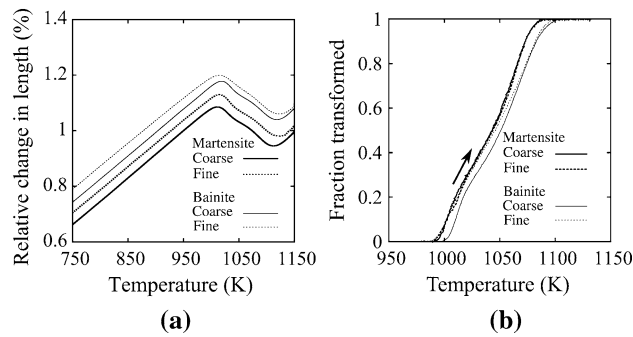


Fig. 6—Evolution of the (a) dilation and (b) austenite fraction measured by dilatometry during the reverse austenite transformation from the four different parent microstructures.

constituents: (i) coarse fresh martensite islands along the prior austenite grain boundary (dashed line) and (ii) lath-shaped particles homogeneously distributed within the tempered martensite microstructure (Figure 7(c)). The location of reverse-transformed austenite grains in the parent coarse bainite is not clearly visible from the micrographs shown in Figure 7(d) where the relatively coarse islands of fresh martensite (light gray areas) are dispersed within large patches of the tempered bainite (TB) appearing dark gray in color with fine cementite particles. The fraction of cementite particles visible within the dark gray area varies between patches as shown in Figure 7(d) and may depend on the orientation between bainite laths and the plane of cut of the micrograph.

The results of EBSD analysis conducted on the coarse martensitic and bainite samples quenched from the intercritical region at 1043 K (770 °C) are summarized in Figure 8. Figures 8(a) and (d) shows the inverse pole figure (IPF) maps including both the bcc and fcc phases. Figures 8(b) and (e) depicts the same area of the sample

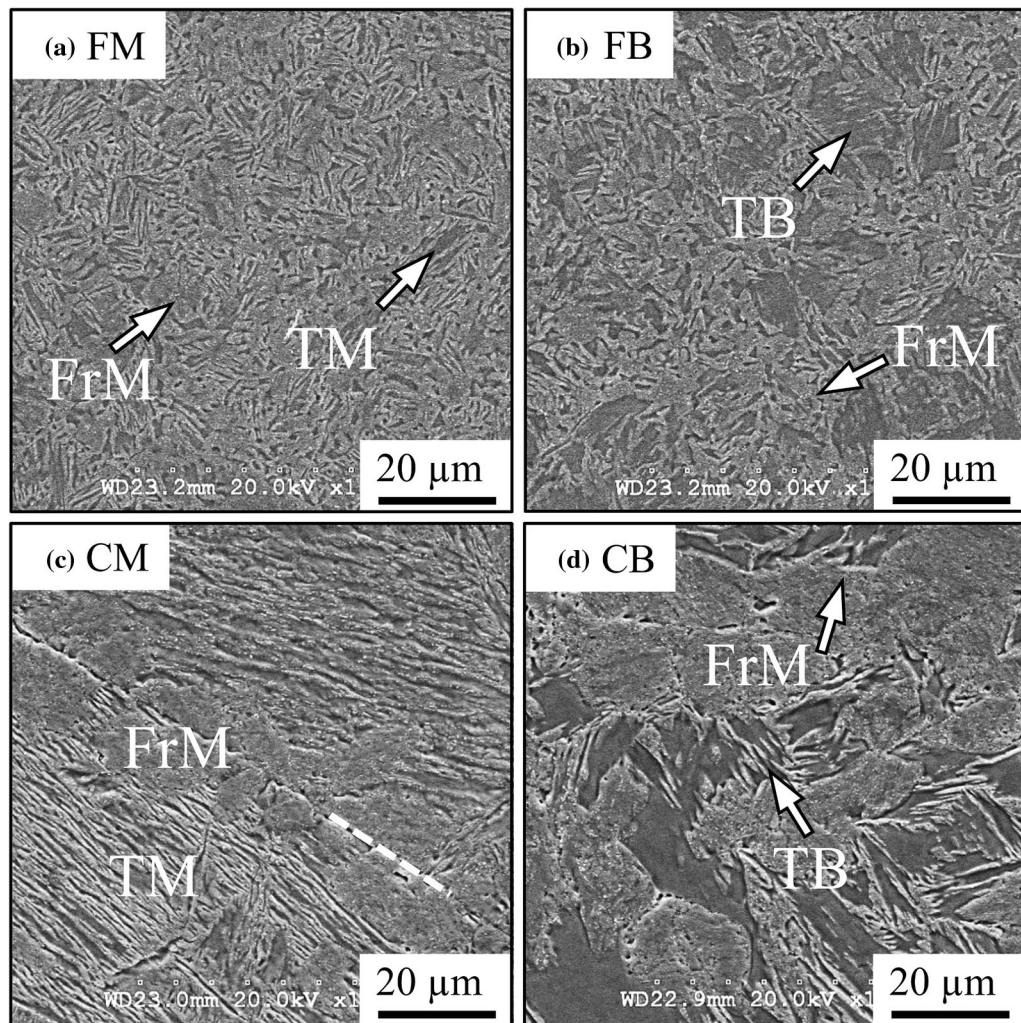


Fig. 7—SEM micrographs of the samples quenched from the intercritical region at a temperature of 1043 K (770 °C) from the parent: (a) fine martensite, (b) fine bainite, (c) coarse martensite, and (d) coarse bainite. FrM indicates fresh martensite (light gray constituent in (a–d) (*i.e.*, intercritical austenite), TM refers to tempered martensite (darker constituent in (a), and TB indicates the tempered bainite (darker constituent in (b) and (d)).

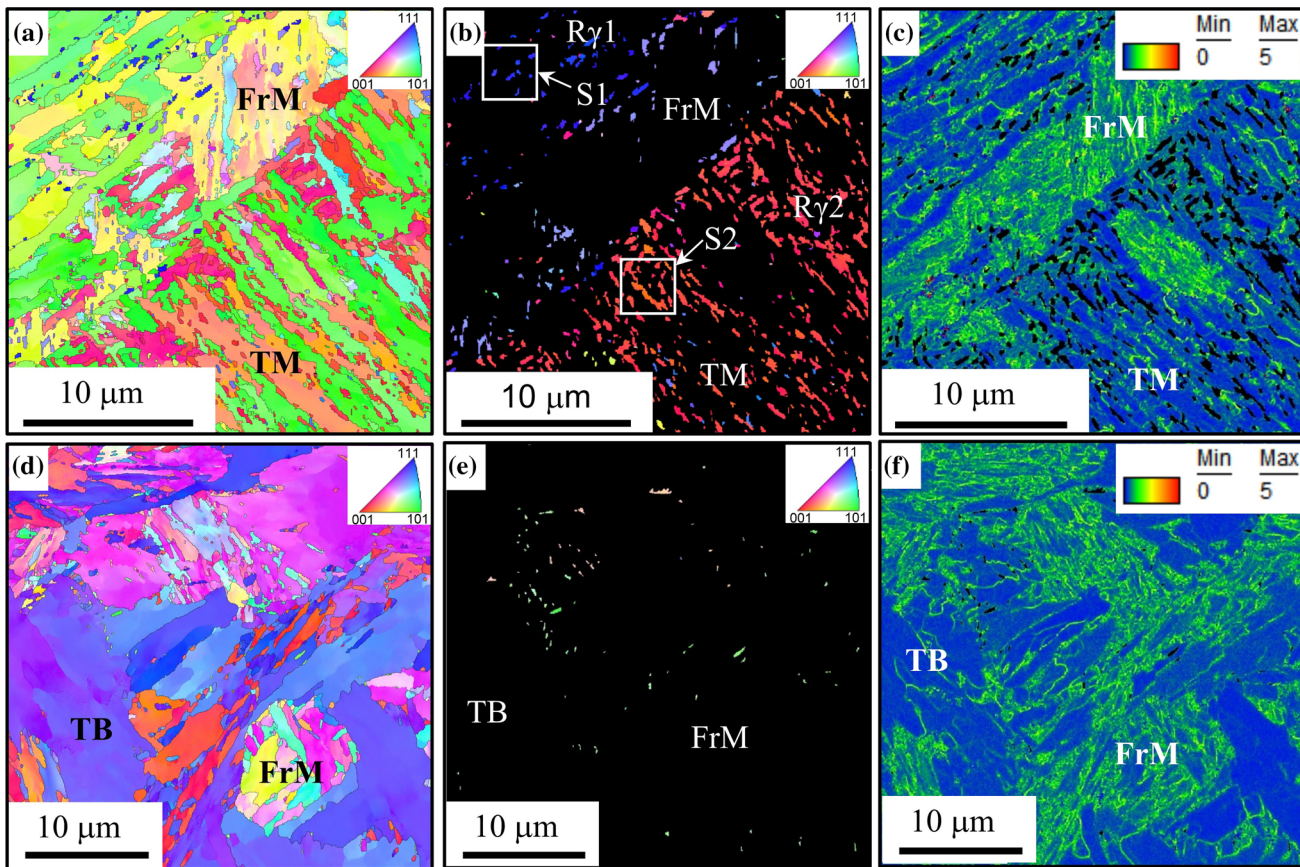


Fig. 8—EBSD scans conducted on samples quenched from 1043 K (770 °C) for the parent coarse martensite (a, b, and c) and coarse bainite (d, e, and f). Figure a and d shows the inverse pole figure (IPF) maps including both bcc and fcc phases. (b) and (e) depicts the same area of the sample with only the fcc phase shown. Figure (c) and (f) shows the Kernel Average Misorientation (KAM) values for the bcc phase. The colors in (a), (b), (d), and (e) correspond to the different crystallographic orientation variants observed in the bcc and fcc phases. The colors in (c) and (f) correspond to the range of KAM values measured on each map.

showing only the fcc phase while excluding the bcc phase. The colors in Figures 8(b) and (e) correspond to the different orientation variants observed in the fcc phase. Figures 8(c) and (f) shows the values of the Kernel Average Misorientation (KAM) for the bcc phase. It is useful to recall at this stage that these intercritically annealed microstructures are composed partially of (i) tempered constituents, *i.e.*, initially present martensite or bainite; (ii) martensite freshly transformed during quenching from the reverse-transformed austenite; and (iii) a small fraction of the retained austenite remaining from the incomplete decomposition of the reverse-transformed austenite. The KAM values offer indirect evidence on the degree of tempering of the phases. High KAM values, *i.e.*, $KAM > 1$ deg (green, yellow, and red in Figures 8(c) and (f)), correspond to the transformation products with a relatively high degree of internal misorientation. In the present situation, these regions are identified as fresh martensite (FrM) transformed from the reverse austenite during quenching from the intercritical region. On the other hand, the areas with low KAM values, *i.e.*, $KAM < 1$ deg (blue in Figures 8(c) and (f)), are representative of the location of tempered martensite (TM) and/or tempered bainite (TB). In the area of

tempered martensite, a relatively large fraction of retained austenite islands are detected in the microstructure after quenching (Figures 8(b)). It is noteworthy that (i) the retained austenite particles possess nearly identical crystallographic orientation when located in the same prior austenite grain and that (ii) they are only detected in the region of tempered martensite where the austenite has reverse transformed between martensite laths—labeled (TM) in Figure 8(c). On the other hand, a negligible fraction of retained austenite is present in the region of fresh martensite. In the case of the parent coarse bainite, the fraction of retained austenite observed after quenching from the intercritical region is much smaller and primarily located within or near the regions of tempered bainite (Figure 8(e)). The KAM values shown in Figure 8(f) provide a good indication about the locations of the regions of fresh martensite (FrM) and tempered bainite (TB). Referring to the IPF map shown in Figure 8(d), the areas of KAM values larger than 1 deg are generally composed of several crystallographic variants of fresh martensite.

In order to evaluate the crystallographic orientations of austenite present under these conditions, the {001} pole figures for the fcc phase are shown in Figures 9(a) and (b) for the parent coarse martensite and bainite,

respectively. Although a large number of retained austenite islands are dispersed in the micrographs shown in Figures 8(b) and (e), the resulting pole figure shows

sharp poles centered around two orientations. Within these two families of orientations, the spread is less than 2 deg. Clearly, if the austenite had nucleated from the

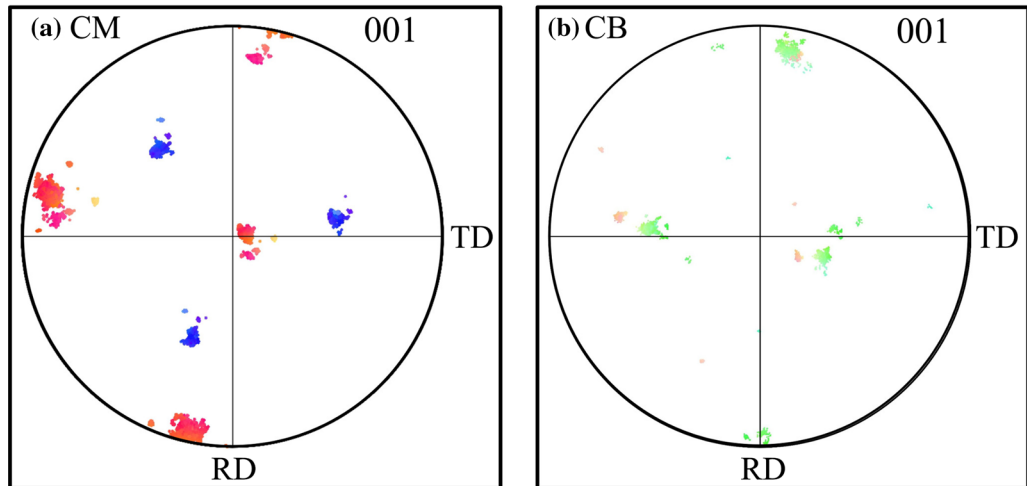


Fig. 9—Pole figure {100} for the fcc phase measured in the samples quenched from 1043 K (770 °C) for the parent coarse martensite (a) and coarse bainite (b).

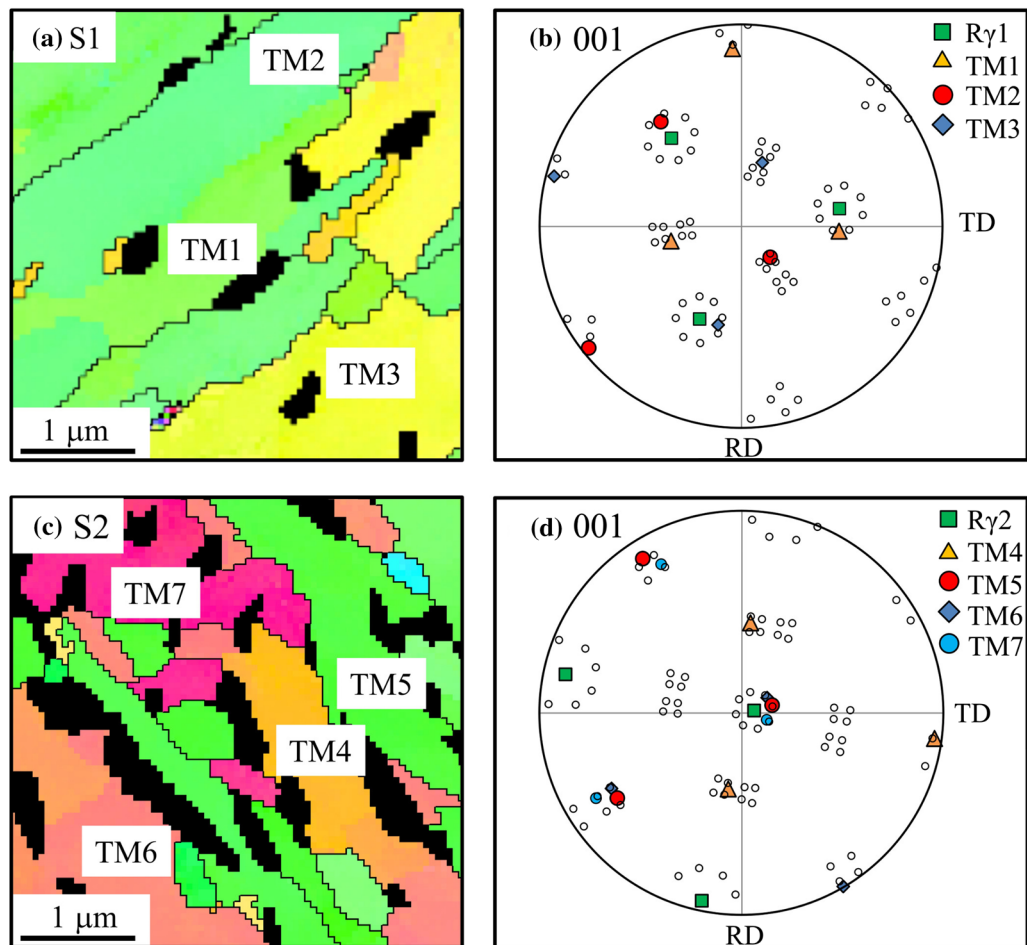


Fig. 10—Selected area of the IPF maps (including only the bcc phase) conducted on the samples quenched from 1043 K (770 °C) for the parent (a) coarse martensite and (c) coarse bainite. {001} pole figures showing the orientation of the retained austenite R γ 1 and R γ 2 present in the (b) coarse martensite and (d) coarse bainite microstructures as highlighted with the white rectangles in (b). The orientations of the TM microstructure constituents are shown and compared with the 24 possible bcc variants resulting from the Kurdjumov–Sachs orientation relationship.

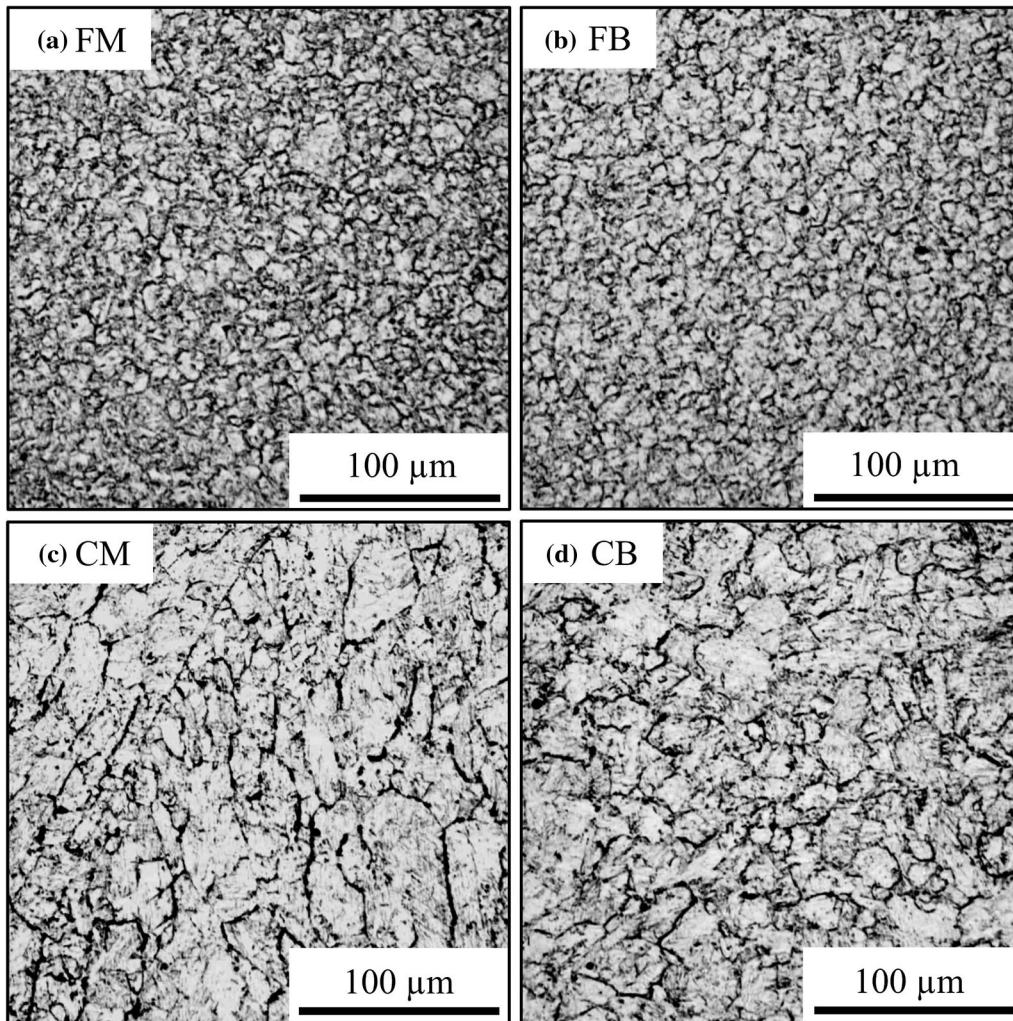


Fig. 11—Optical micrographs of the samples quenched from the onset of the austenite temperature domain at 1123 K (850 °C) for the (a) parent fine martensite, (b) parent fine bainite, (c) parent coarse martensite, and (d) parent coarse bainite.

martensite at different locations, several variants of orientation would be present after quenching from the intercritical region. Instead, all the austenite islands found in this condition possess nearly the same orientation when located in the same prior austenite grain. One can therefore conclude that the reverse austenite formation starts from the retained austenite initially present.

To confirm this hypothesis, one can identify the orientation relationships between the tempered martensite laths and the retained austenite. Two areas are selected for this purpose in the EBSD scans in Figure 8(b), being shown as highlighted with white rectangles. The area S1 is selected from the area in which the retained austenite orientation is $R\gamma_1$, and the other area S2, selected from the area in which the retained austenite orientation is $R\gamma_2$. The bcc IPF maps of the areas S1 and S2 are shown in Figures 10(a) and (c), respectively. Figures 10(b) and (d) provides the corresponding $\{001\}$ pole figures where the average orientation of the retained austenite is shown by square symbols. In these two pole figures, the 24 crystallographic variants defined by the Kurdjumov–Sachs

(K–S) orientation relationships^[66] and calculated from the orientations $R\gamma_1$ and $R\gamma_2$ are indicated with open circle symbols. Several variants (from TM1 to TM7) of the tempered martensite are then positioned in these two pole figures. Clearly, all the variants of tempered martensite observed in the selected areas are in K–S orientation relationships with the corresponding retained austenite. This observation confirms that the austenite present in this intercritically quenched sample is initially present in the parent microstructure and that no nucleation is required for the reverse transformation under this condition.

D. Austenite Grain Growth

Figure 11 shows optical micrographs of the samples quenched from the onset of the fully austenitic region at 1123 K (850 °C) for the parent fine martensite and bainite (Figures 11(a) and (b)), as well as for the coarse martensite and bainite (Figures 11(c) and (d)), respectively. The austenite grain boundaries are clearly visible in all micrographs allowing for the quantitative analysis

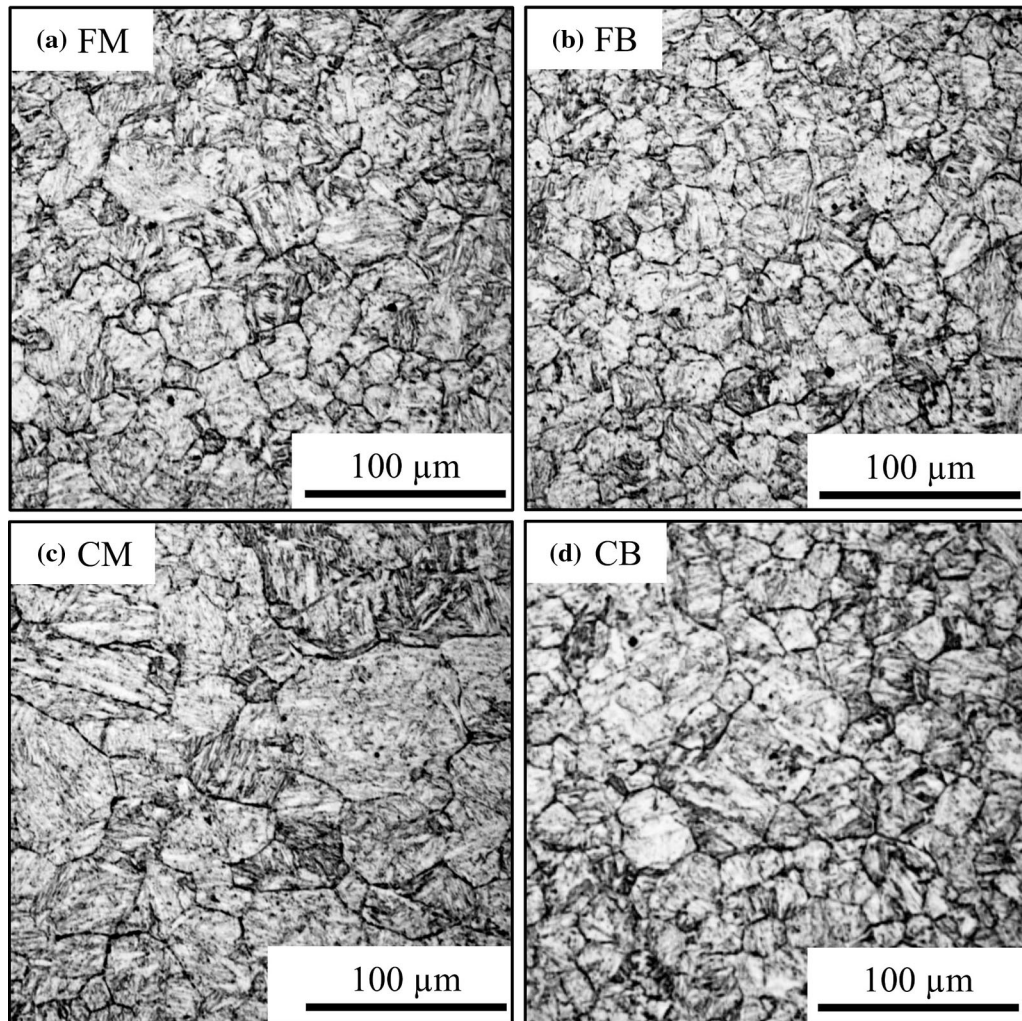


Fig. 12—Optical micrographs of the samples quenched from the peak temperature of 1273 K (1000 °C) for the (a) parent fine martensite, (b) parent fine bainite, (c) parent coarse martensite, and (d) parent coarse bainite.

of the mean grain size. The austenite grains have an EQADs of 4 μm and 3 μm , respectively, for the parent fine martensite and fine bainite. On the other hand, the austenite grain size is 22 μm for the coarse martensite and 14 μm for the coarse bainite. This observation suggests that the initial austenite structure (*i.e.*, coarse or fine) is to some degree recovered through the mechanisms of austenite formation upon re-heating. Figure 12 shows the optical micrographs of the samples quenched at the end of the second reheating cycle, *i.e.*, at 1273 K (1000 °C), for the parent fine martensite and bainite (Figures 12(a) and (b)), as well as for the coarse martensite and bainite (Figures 12(c) and (d)). All cases show a microstructure composed of polygonal austenite grains with a rather homogeneous distribution in size. The mean austenite grain sizes are 40 μm for the coarse martensite, 29 μm for the coarse bainite, 31 μm for the fine martensite, and 17 μm for the fine bainite.

The evolution of the austenite grain size, measured continuously by laser ultrasonics during the 2nd stage of the heating cycle, is shown in Figure 13 for each of the four parent microstructures. Thick lines depict the

evolution of grain size from the coarse martensite (solid line) and fine martensite (dotted line). Thin lines depict the evolution of the austenite grain size when transformed from the coarse bainite (solid line) and fine bainite (dotted line). The metallographically measured grain sizes are shown with symbols in Figure 13. Acceptable agreement is found between the two techniques validating the reliability of the LUMet technology under these conditions. Further, the LUMet measurements provide fast and continuous information on the growth rate for each condition. First, the austenite grain size is initially finer when transformed from the two fine parent microstructures. In the case of the fine bainite, the growth rate remains relatively slow in the investigated temperature region. In contrast, the growth rate measured for the austenite grains transformed from the parent fine martensite is much more pronounced at temperatures above 1223 K (950 °C). In the cases of the parent coarse bainite and martensite, the rates of growth are equivalent, and the final austenite grain size at the peak temperature remains smaller for the sample with the parent bainite microstructure.

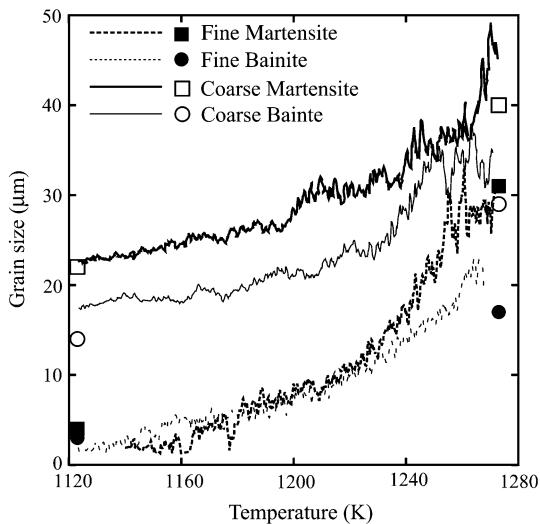


Fig. 13—Evolution of the austenite grain size measured using laser ultrasonics during continuous heating at a rate of 0.3 K/s from the parent coarse martensite (thick continuous line) and fine martensite (thick dotted line) as well as from the parent coarse bainite (thin continuous line) and parent fine bainite (thin dotted line). Metallographic grain sizes are indicated with open and closed symbols.

Clearly, the differences observed for the initial austenite grain size at 1123 K (850 °C) in these four scenarios is strongly related to the mechanisms involved in the reverse transformation of austenite. On the other hand, the differences measured in the rates of growth for these cases are intimately linked to the effective driving pressure for growth, *i.e.*, grain boundary curvature and potential precipitate pinning of grain boundaries.

IV. DISCUSSION

The coupling of *ex-situ* metallography and real-time laser ultrasonic inspection provides complementary information on the occurrence of the reverse austenite transformation and the subsequent austenite grain growth. The initial austenite grain size at the completion of the reverse austenite transformation is largely affected by the features of the parent microstructure. In the cases of the parent fine martensite and fine bainite, a small austenite grain size is observed at the completion of austenite formation. The reverse austenite transformation is initiated from retained austenite constituents and by nucleation of reverse austenite at prior austenite grain boundaries and cementite particles, and the subsequent migration of the austenite interfaces are governed by the redistribution of carbon. The starting mechanism for the reverse austenite transformation for the parent coarse martensite is similar to that observed for the parent fine martensite. The close crystallographic orientations of the retained austenite particles initially present in the parent microstructures contribute to the partial coarsening of the austenite grains at the completion of the reverse austenite transformation, thereby leading to the formation of a coarse austenite grain

structure. In the case of the parent coarse bainite microstructure, the presence of cementite in the structure also contributes to the formation of new variants of austenite, thus limiting the coarsening of the austenite grains at the completion of the reverse transformation.

The differences observed in the rates of austenite grain growth cannot be solely explained by the various mechanisms involved during the austenite formation. The reverse transformation has an influence on the initial size of the austenite grains and therefore governs the initial curvature of the grain boundaries.^[67] The rate of growth is inversely proportional to the grain boundary curvature and is known to be strongly affected by the presence of nanometric precipitates pinning the boundaries and slowing down their migration.^[68] Laser ultrasonic grain-size measurements show that for approximately the same initial grain curvature, the growth rate measured for the parent fine martensite is larger than that measured in the parent fine bainite microstructure. In addition, a similar growth rate is observed for the fine and coarse bainite samples. These observations suggest that the growth rate is also affected by the particle pinning. Additional TEM analysis was conducted in the CM and CB samples quenched from 1273 K (1000 °C). The thin foil TEM image of the CB sample shown in Figure 14(a) confirms the presence of nanometric AlN precipitates, as identified by local EDX analysis (Figure 14(b)) on the three separate particles indicated by arrows. In contrast, no such precipitates are observed in the imaged areas of the CM sample, and this observation is also consistent with the TEM results obtained at 953 K (680 °C), *i.e.*, before the onset of the reverse austenite transformation in the case of CM (see Figure 5). Thus, it can be concluded that AlN precipitates are either not present or their particle density is much lower than that in the CB sample. The typical size of the AlN particles in the CB microstructure is approximately 50 nm. The difference in the heat treatments of CB and CM samples is the holding at 773 K (500 °C) which may promote AlN formation. According to previous studies,^[69–71] the precipitation rates of AlN particles are, however, very low in ferrite at 773 K (500 °C) (equilibrium fraction reached after 10⁷ s at 773 K in a steel with 0.46 wt pct Al and 0.0067 wt pct N^[70]). Precipitation of AlN in bainite may be accelerated due to the presence of a higher dislocation density. Further, previous studies suggest that some particle coarsening can occur during re-heating at a rate of 0.3 K/s from 973 K (700 °C) to 1273 K (1000 °C).^[72,73] The pinning pressure of AlN precipitates can effectively control the growth kinetics of the reverse-transformed austenite grains as previously observed by numerous experimental studies.^[74–76] The presence of AlN at 1273 K (1000 °C) for the investigated steel chemistry is further confirmed by Thermocalc (TCFE7 database) calculations indicating an equilibrium fraction of AlN of 0.009 in austenite at 1273 K (1000 °C) and a solution temperature of 1573 K (1300 °C). One can therefore infer that the precipitation of AlN particles is stimulated by holding at 773 K (500 °C) but continues to occur during the reverse austenite transformation upon re-heating. The observation of the presence of AlN

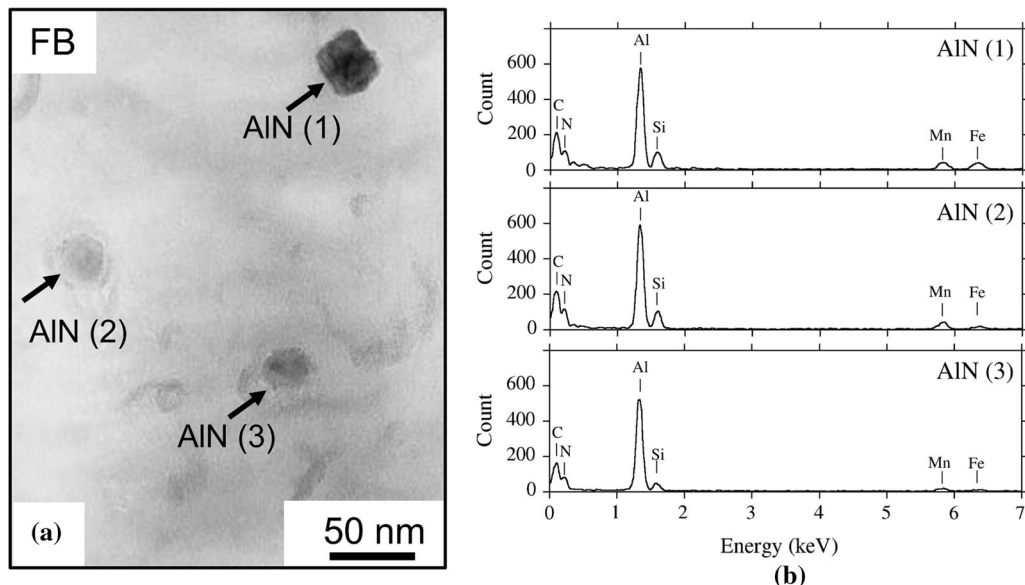


Fig. 14—(a) TEM image of the parent coarse bainite sample quenched from 1273 K (1000 °C). (b) EDX spectrum of the AlN particles observed in the TEM image.

particles in the CB sample provides a qualitative rationale for the lower austenite grain growth rates in samples with initial bainite microstructures compared with initial martensite microstructures.

V. SUMMARY

The reverse austenite transformation behavior as well as the subsequent grain growth was investigated in low-carbon steels with different parent microstructures. The mechanisms governing the reverse austenite transformation upon re-heating were examined by dilatometry and *ex-situ* metallography. The subsequent grain growth was *in situ* measured by laser ultrasonics. The austenite formation temperature is only weakly affected by the initial microstructure, but the grain size at the completion of austenite formation strongly depends on the initial microstructure. A smaller austenite grain structure is obtained when transforming from a parent bainite microstructure, where the cementite particle serve as new nucleation site for austenite. The presence of AlN precipitates in the parent bainite structure is playing an important role in controlling the austenite grain growth rate. In summary, this study indicates that the generation of a bainitic microstructure during the acceleration of cooling promotes the formation of a fine austenite structure upon the subsequent slow reheating.

ACKNOWLEDGMENTS

The financial contributions from the Canadian Foundation of Innovation (CFI) and the Natural Science and Engineering Research Council (NSERC) of Canada are gratefully acknowledged.

REFERENCES

1. K. Araki, T. Yuasa, and Y. Tamura: Technical Report, JFE Steel Corporation, Kawasaki-cho, Chuo-ku, Chiba, Japan, 2013, vol. 18, pp. 56–62.
2. K. Ueda A. Ohmori S. Endo N. Shikanai: *Curr. Adv. Mater. Process: ISIJ*, 2007, vol. 20 (3), p. 465.
3. R.R. Judd and H.W. Paxton: *Trans. Metall. Soc. AIME*, 1968, vol. 242, pp. 206–14.
4. M. Hillert, K. Nilsson, and L.E. Törndahl: *J. Iron. St. Inst.*, 1971, vol. 209, pp. 49–65.
5. N.C. Law and D.V. Edmonds: *Metall. Mater. Trans. A.*, 1980, vol. 33, pp. 33–46.
6. G.R. Speich, V.A. Demarest, and R.L. Miller: *Metall. Trans. A.*, 1981, vol. 12, pp. 1419–28.
7. C.I. Garcia and A.J. Deardo: *Metall. Mater. Trans. A*, 1981, vol. 12, pp. 521–30.
8. D.Z. Yang, E.L. Brown, D.K. Matlock, and G. Grauss: *Metall. Trans. A*, 1985, vol. 16, pp. 1385–92.
9. C. Garcia de Andrés, F.G. Caballero, and C. Capdevila: *Scr. Mater.*, 1998, vol. 39, pp. 791–96.
10. D.V. Shtansky, K. Nakai, and Y. Ohmori: *Acta Mater.*, 1999, vol. 47, pp. 2619–32.
11. F.G. Caballero, C. Capdevila, and C. Garcia de Andrés: *Scr. Mater.*, 2000, vol. 42, pp. 1159–65.
12. F.G. Caballero, C. Capdevila, and C. Garcia de Andrés: *Mater. Sci. Technol.*, 2001, vol. 17, pp. 1114–18.
13. F.G. Caballero, C. Capdevila, and C. Garcia de Andrés: *ISIJ Int.*, 2001, vol. 41, pp. 1093–102.
14. F.G. Caballero, C. Capdevila, and C. Garcia de Andrés: *Metall. Mater. Trans. A*, 2001, vol. 32, pp. 1283–91.
15. C. Zhang, L. Zhou, X. Liu, X. Wu, and Y. Liu: *Steel Res. Int.*, 2014, vol. 85 (10), pp. 1453–58.
16. S.D. Martín, T. de Cock, A. García-Junceda, F.G. Caballero, C. Capdevila, and C.G. de Andrés: *Mater. Sci. Technol.*, 2008, vol. 24(3), pp. 266–72.
17. H. Azizi-Alizamini, M. Militzer, and W.J. Poole: *Metal. Mater. Trans. A*, 2011, vol. 42, pp. 1544–57.
18. G. Molinder: *Acta Metall.*, 1956, vol. 4, pp. 565–71.
19. R.C. Reed, Z. Shen, T. Akbay, and J.M. Robinson: *Mater. Sci. Eng. A*, 1997, vol. 232, pp. 140–49.
20. R.C. Reed, T. Akbay, Z. Shen, J.M. Robinson, and J.H. Root: *Mater. Sci. Eng. A*, 1998, vol. 256, pp. 152–65.
21. Q. Lai, M. Goune, A. Perlade, T. Pardoën, P. Jacques, O. Bouaziz, and Y. Bréchet: *Metal. Mater. Trans. A*, 2016, vol. 47, pp. 3375–86.

22. J.J. Yi, I.S. Kim, and H.S. Choi: *Metall. Trans. A.*, 1985, vol. 16, pp. 1237–45.
23. J.R. Yang: *Mater. Sci. Eng. A*, 1991, vol. 131, pp. 99–113.
24. J.R. Yang and H.K.D.H. Bhadeshia: *Mater. Sci. Eng. A*, 1991, vol. 131, pp. 99–113.
25. C. Philippot, J. Drillet, P. Maugis, V. Hebert, and M. Dumont: *Metall. Res. Technol.*, 2014, vol. 111 (1), pp. 3–8.
26. E. López-Martínez, O. Vázquez-Gómez, H.J. Vergara-Hernández, and B. Campillo: *Int. J. Miner. Metall. Mater.*, 2015, vol. 22 (12), pp. 1304–12.
27. J. Huang, W.J. Poole, and M. Militzer: *Metal. Mater. Trans. A*, 2004, vol. 35, pp. 3363–75.
28. M. Kulakov, W.J. Poole, and M. Militzer: *Metal. Mater. Trans. A*, 2013, vol. 44, pp. 3564–76.
29. A. Chbihi, D. Barbier, L. Germain, A. Hazotte, and M. Gouné: *J. Mater. Sci.*, 2014, vol. 49 (10), pp. 3608–21.
30. D. Barbier, L. Germain, A. Hazotte, M. Gouné, and A. Chbihi: *J. Mater. Sci.*, 2015, vol. 50 (1), pp. 374–81.
31. Y. Mazaheri, A. Kermanpur, A. Najafizadeh, and A.G. Kalashami: *Metall. Mater. Trans. A*, 2016, vol. 47 (3), pp. 1040–51.
32. D.-W. Suh, C.-S. Oh, and S.-J. Kim: *Met. Mater. Int.*, 2008, vol. 14 (3), pp. 275–82.
33. P. Li, J. Li, Q. Meng, W. Hu, and D. Xu: *J. Alloys Compd.*, 2013, vol. 578, pp. 320–27.
34. P. Li, J. Li, Q. Meng, W. Hu, and D. Xu: *Ironmak. Steelmak.*, 2015, vol. 42 (2), pp. 81–87.
35. G. Liu, J. Li, S. Zhang, J. Wang, and Q. Meng: *J. Alloys Compd.*, 2016, vol. 666, pp. 309–16.
36. N. Li, J. Lin, D.S. Balint, and T.A. Dean: *J. Mater. Process. Technol.*, 2016, vol. 237, pp. 254–64.
37. A. Karmakar, M. Ghosh, and D. Chakrabarti: *Mater. Sci. Eng. A*, 2013, vol. 564, pp. 389–99.
38. F. Fazeli and M. Militzer: *J. Iron Steel Res. Int.*, 2011, vol. 18 (1–2), pp. 658–63.
39. H. Farahani, W. Xu, and S. van der Zwaag: *Metall. Mater. Trans. A*, 2015, vol. 46 (11), pp. 4978–85.
40. C. Zheng and D. Raabe: *Acta Mater.*, 2013, vol. 61 (14), pp. 5504–17.
41. H. Azizi-Alizamini and M. Militzer: *Int. J. Mater. Res.*, 2010, vol. 101, pp. 534–41.
42. B. Zhu and M. Militzer: *Metal. Mater. Trans. A*, 2015, vol. 46, pp. 1073–84.
43. M. Kulakov, W.J. Poole, and M. Militzer: *ISIJ Int.*, 2014, vol. 54, pp. 2627–26.
44. N. Li, J. Lin, D.S. Balint, and T.A. Dean: *J. Mater. Process. Technol.*, 2016, vol. 237, pp. 394–401.
45. H. Li, K. Gai, L. He, C. Zhang, H. Cui, and M. Li: *Mater. Des.*, 2016, vol. 92, pp. 731–41.
46. Y.-K. Lee, H.C. Shin, D.S. Leem, J.-Y. Choi, W. Jin, and C.S. Choi: *Mater. Sci. Technol.*, 2003, vol. 19, pp. 393–98.
47. T. Shirane, S. Tsukamoto, K. Tsuzaki, Y. Adachi, T. Hanamura, M. Shimizu, and F. Abe: *Sci. Technol. Weld. Joining*, 2009, vol. 14, pp. 698–707.
48. S.T. Kimmins and D.J. Gooch: *Metal Sci.*, 1983, vol. 17, pp. 519–32.
49. T. Hara, N. Maruyama, Y. Shinohara, H. Asahi, G. Shigesato, M. Sugiyama, and T. Koseki: *ISIJ Int.*, 2009, vol. 49 (11), pp. 1792–1800.
50. C. Wang, R. Fu, and W. Zhou: *Mater. Sci. Eng., A*, 2006, vols. 438–440, pp. 1135–38.
51. V.D. Sadovskii, N.M. Rodigin, L.V. Smirnov, G.M. Filonchik, and I.G. Fakidov: *Fiz. Metal. Metalloved.*, 1961, vol. 12, p. 302.
52. T. Kakeshita and T. Saburi: *Met. Mater.*, 1997, vol. 3 (2), pp. 87–96.
53. N. Nakada, T. Tsuchiyama, S. Takaki, and S. Hashizume: *ISIJ Int.*, 2007, vol. 47 (10), pp. 1527–32.
54. S. Watanabe and T. Kunitake: *Tetsu to Hagane*, 1975, vol. 61, pp. 96–106.
55. S.J. Davies, C. Edwards, G.S. Taylor, and S.B. Palmer: *J. Phys. D*, 1993, vol. 26, pp. 329–48.
56. J.P. Monchalín: *Rev. Quant. Nondestruct. Eval.*, 2004, vol. 23, pp. 3–31.
57. M. Dubois, M. Militzer, A. Moreau, and J.F. Bussière: *Scripta Mater.*, 2000, vol. 42, pp. 867–74.
58. S. Kruger, G. Lamouche, J.P. Monchalín, R. Kolark, G. Jeskey, and M. Choquet: *Iron Steel Technol.*, 2005, vol. 2, pp. 25–31.
59. S. Sarkar, A. Moreau, M. Militzer, and W.J. Poole: *Metall. Mater. Trans., A*, 2008, vol. 39, 897–907.
60. M. Maalekian, R. Radis, M. Militzer, A. Moreau, and W.J. Poole: *Acta Mater.*, 2012, vol. 60, pp. 1015–26.
61. S.E. Kruger and E.B. Damm: *Mater. Sci. Eng. A*, 2006, vol. 425, pp. 238–43.
62. A. Moreau, D. Lévesque, M. Lord, M. Dubois, J.P. Monchalín, C. Padioléau, and J.F. Bussière: *Ultrasonics*, 2002, vol. 40, pp. 1047–56.
63. T. Garcin, J.H. Schmitt, and M. Militzer: *J. Alloys Compd*, 2016, vol. 670, pp. 329–36.
64. T. Garcin: CTOME V1.56: Software for the Analysis of Ultrasound Wave Properties in Metal. www.ctome.org.
65. ASTM A1033-10: Standard Practice for Quantitative Measurement and Reporting of Hypoeutectoid Carbon and Low-Alloy Steel Phase Transformations. ASTM International, West Conshohocken, PA, 2015, www.astm.org.
66. Z. Nishiyama: Martensite transformation, 1978, Academic press Inc, New York, ISBN 0-12-519850-7.
67. T. Gladman: *The Physical Metallurgy of Microalloyed Steels*, The Institute of Materials, London, 2002, pp. 137–84.
68. T. Gladman: *Heat Treatment of Metals (UK)*, 1994, vol. 21, pp. 11–14.
69. R. Radis and E. Kozeschnik: *Modelling Simul. Mater. Sci. Eng.*, 2010, vol. 18, p. 055003.
70. A. Brahmi and R. Borelli: *Acta Mater.*, 1997, vol. 45, pp. 1889–97.
71. V. Massardier, V. Guetaz, J. Merlin, and M. Solar: *Mater. Sci. Eng. A*, 2003, vol. 355, pp. 299–310.
72. L.M. Cheng, E.B. Hawbolt, and T.R. Meadowcroft: *Metall. Mater. Trans. A*, 2000, vol. 31, pp. 1907–16.
73. L.M. Cheng, E.B. Hawbolt, and T.R. Meadowcroft: *Scr. Mater.*, 1999, vol. 41, pp. 673–78.
74. M. Militzer, A. Giumelli, E.B. Hawbolt, and T.R. Meadowcroft: *Metall. Mater. Trans. A*, 1996, vol. 27, pp. 3399–409.
75. N. Gao and T.N. Baker: *ISIJ Int.*, 1998, vol. 18, pp. 744–51.
76. G.R. Speich, J. Cuddy, C.R. Gordan and A.J. DeArdo, Phase Transformation in Ferrous Alloys (Warrendale, PA: The Metallurgical Society of AIME) pp. 341–89.